Materials Advances

ROYAL SOCIETY OF CHEMISTRY

PAPER

View Article Online
View Journal | View Issue

Cite this: *Mater. Adv.*, 2026, 7, 3276

Thermal and gamma-ray-induced density dilution in orthoferrosilite ($FeSiO_3$): implications for photon shielding stability

Z. Y. Khattari

Orthoferrosilite ($FeSiO_3$), an iron-rich orthopyroxene, was investigated for its structural stability and photon attenuation performance under thermal and gamma-ray environments. This work provides the first quantitative linkage between temperature-dependent polyhedral expansion—specifically the pronounced dilation of FeO_6 octahedra *versus* rigid SiO_4 tetrahedra—and the resulting degradation in gamma-ray shielding efficiency. Unlike prior studies that treat shielding degradation as a bulk density effect, we establish a crystal-chemical mechanism directly correlating atomic-scale thermal response to macroscopic photon attenuation loss. High-temperature X-ray diffraction analysis revealed a density decrease of approximately 3.2% between 25 °C and 800 °C, driven primarily by the pronounced thermal expansion of FeO_6 octahedra compared to the minimal contraction of SiO_4 tetrahedra. Gamma radiation further reduced density, leading to a LAC by up to 9% at 1 MeV for the highest dose tested. Despite volumetric changes, the effective atomic number ($Z_{eff} \approx 21.5$) and electron density ($N_{eff} \approx 3.2 \times 10^{23}$ e cm^{-3}) remained constant, confirming that shielding degradation stems solely from density dilution, not altered interaction probabilities. A key distinction is established: thermally-induced expansion is largely reversible, whereas gamma-induced damage involves athermal defect accumulation with potential irreversibility—a critical insight for predicting long-term shielding performance in mixed-field environments. These results highlight the importance of microstructural stability for orthoferrosilite-based shielding in environments subject to thermal cycling or prolonged irradiation, and suggest pathways for material optimization through compositional tuning and composite design.

Received 4th January 2026,
Accepted 18th February 2026

DOI: 10.1039/d6ma00013d

rsc.li/materials-advances

1. Introduction

The safe management of ionizing radiation is a cornerstone technology for nuclear energy, radiotherapy, and the exploration of space.[1] For decades, this protection has relied on dense, high-atomic-number materials like lead and specialized concrete.[2–4] While effective, these solutions present significant limitations. Lead's toxicity and weight complicate handling and disposal, posing persistent environmental and health risks.[5,6] Concrete, though versatile, can degrade under the combined effects of radiation flux and thermal cycling, leading to a loss of structural integrity over time.[7,8] This landscape has driven a concerted search for next-generation shielding materials that are non-toxic, lightweight, and inherently stable under operational stresses, particularly high temperature.[9–11]

In response, research has expanded into advanced ceramics and glass-ceramics.[9] A consistent finding across multiple studies is that composition directly dictates shielding performance.[1] For instance, silicate glass-ceramics derived from basalt show a clear increase in gamma attenuation with higher basalt content.[12] Similarly, systematic studies on borate-tellurite glasses reveal that raising the concentration of modifier oxides like MgO enhances density and improves shielding parameters.[13] This principle extends to bioactive silicate glasses, where specific compositional shifts to include Na_2O and P_2O_5 create dual-purpose materials capable of both optical, medical integration and radiation protection.[14] Parallel efforts have extensively validated the correlation between density and linear attenuation coefficient in amorphous oxide systems—including Bi_2O_3-doped phosphate glasses and MO-doped borate glasses—using computational toolkits such as Phy-X/PSD and MCNP.[14–18] These studies confirm that compositional tuning of density directly enhances photon attenuation, a principle we now extend to crystalline silicates. The collective evidence underscores that calcium-magnesium-silicate systems, whether in amorphous or crystalline form, constitute a highly viable foundation for developing effective, lead-free radiation barriers.[8–14] Very recent investigations have further advanced oxide-based shielding: rare earth-doped borate glasses, transition metal oxide-tellurite, NiO-borates, and

Department of Physics, Faculty of Science, The Hashemite University, P. O. Box 330127, Zarqa 13133, Jordan. E-mail: zkhattari@hu.edu.jo

Bi_2O_3 glasses demonstrate composition-dependent attenuation enhancement.[15] Extending to silicate-based systems, Cr^{3+}-doped $Ba(La)_2SiO_6$ glass-ceramics show validated MAC,[16] while TiO_2-enhanced phosphate glasses achieve linear attenuation coefficients up to 19.795 cm^{-1}. These advances motivate the present investigation into crystalline orthoferrosilite, where anisotropic thermal response offers distinct advantages over amorphous networks.

Within this material class, orthopyroxene minerals offer a uniquely advantageous crystalline structure for applications involving elevated temperatures.[19] These silicates, with the general formula $XYSi_2O_6$ (X/Y is a cation), can incorporate various cations while maintaining a robust orthorhombic (*Pbca*) framework. Orthoferrosilite ($FeSiO_3$), the iron-rich end-member, is a prime exemplar. It exhibits remarkable thermal stability, maintaining its *Pbca* structure without phase transformation from room temperature up to at least 980 °C.[20] Crucially, its lattice does not simply expand uniformly with heat; it undergoes specific, anisotropic structural adjustments. These include a significant lengthening of the Fe–O bonds and a straightening of the linked silicate tetrahedral chains, which alters the overall atomic packing and electron density distribution within the crystal.[21] The presence of Fe^{2+} cations further enhances its intrinsic photoelectric absorption at lower gamma energies. These characteristics make orthoferrosilite an exceptional model system for probing the fundamental relationship between thermally induced lattice dynamics and radiation shielding efficiency.[22]

Despite this potential, critical questions remain unanswered. The explicit link between thermal expansion metrics—such as the increase in Fe–O bond lengths or the widening of key oxygen angles—and changes in gamma-ray attenuation cross-sections has not been established. It is unknown whether the shielding performance evolves uniformly across the photon energy spectrum or if improvements are localized to specific interaction regimes (*e.g.*, photoelectric effect) due to these structural changes.[23] Furthermore, the quantitative performance of a high-temperature mineral like orthoferrosilite must be benchmarked against conventional and emerging shields under simulated thermal operating conditions to assess its practical utility.[24]

This study directly addresses these gaps by merging high-temperature crystallographic data with computational radiation transport modeling. We utilize detailed structural parameters of orthoferrosilite determined across a temperature range from 24 °C to 980 °C. This data quantifies the material's anisotropic expansion and the specific geometric evolution of its polyhedral chains.[24] These temperature-dependent structural models then serve as direct inputs for simulations using the established Geant4 Monte Carlo toolkit to compute the linear and mass attenuation coefficients across a broad energy range (0.01–10 MeV) for each temperature state. Our integrated analysis demonstrates how the crystal lattice's response to heat directly modulates its photon-stopping power, validating the concept of an intrinsically temperature-responsive crystalline shield. By decoding the connection between atomic-scale thermal motion and macroscopic shielding properties, this work provides a new paradigm for engineering solid-state radiation barriers that are optimized for stability and performance in high-temperature environments.

2. Materials and methods

2.1. Sample selection and crystallographic data

This study focuses on the temperature-dependent gamma-ray shielding properties of the orthopyroxene orthoferrosilite ($FeSiO_3$). The investigation utilizes crystallographic information files (CIFs)[25] for the orthorhombic phase (space group *Pbca*, #61) at temperatures of 24, 400, 600, 800, 900, and 980 °C[19], and for the monoclinic phase (space group *C*2/*c*, #15) at 1050 °C.[26] These CIFs, with reference codes provided in Table 1, were sourced from the Crystallography Open Database (COD).[27]

The original high-temperature X-ray diffraction experiments were conducted by Sueno *et al.*[19] using a synthetic single crystal of orthoferrosilite ($FeSiO_3$) mounted on a Picker four-circle diffractometer equipped with a gas-flow high-temperature furnace. Diffraction intensities were measured at each target temperature using MoK_α radiation (λ = 0.71069 Å). The crystal was heated stepwise from 24 °C to 980 °C, with data collections performed at 400, 600, 800, 900, and 980 °C. At each temperature step, the crystal was allowed to thermally equilibrate for approximately 30–60 minutes prior to intensity measurement, with temperature stability maintained within ±5 °C. Lattice parameters were refined by least-squares fitting of 12–15

Table 1 Temperature-dependent crystal structure parameters of orthoferrosilite ($FeSiO_3$) in the orthorhombic system (space group *Pbca* [#61]) between 24 °C ≤ *T* ≤ 980 °C, and in the monoclinic system (space group *C*2/*c* [#15]) at 1050 °C[19] is shown in the Table. The listed parameters include lattice constants (*a*, *b*, *c*), unit cell volume (V_c), density (ρ), and atomic packing fraction (APF), with corresponding CIF reference codes obtained from the Crystallography Open Database (COD).[27] A progressive lattice expansion with increasing temperature is observed, accompanied by decreasing density and APF values, indicating thermal-induced structural relaxation. The number of formula units per cell is *Z* = 16 for 24 °C ≤ *T* ≤ 980 °C and *Z* = 8 at 1050 °C

	Lattice parameters (Å)						
Temperature (°C)	*a*	*b*	*c*	V_c (Å^3)	ρ (g cm^{-3})	APF	CIF refcode
24	18.418	9.078	5.2366	875.552	4.00351	0.66807	9000476
400	18.484	9.124	5.2593	886.971	3.95197	0.65947	9000477
600	18.527	9.145	5.2756	893.842	3.92159	0.6544	9000478
800	18.569	9.160	5.2974	901.046	3.89023	0.64917	9000479
900	18.596	9.1685	5.3113	905.563	3.87083	0.64593	9000480
980	18.614	9.172	5.3199	908.254	3.85936	0.64402	9000481
1050	9.928	9.179	5.338	456.527	3.83907	0.64063	9000917

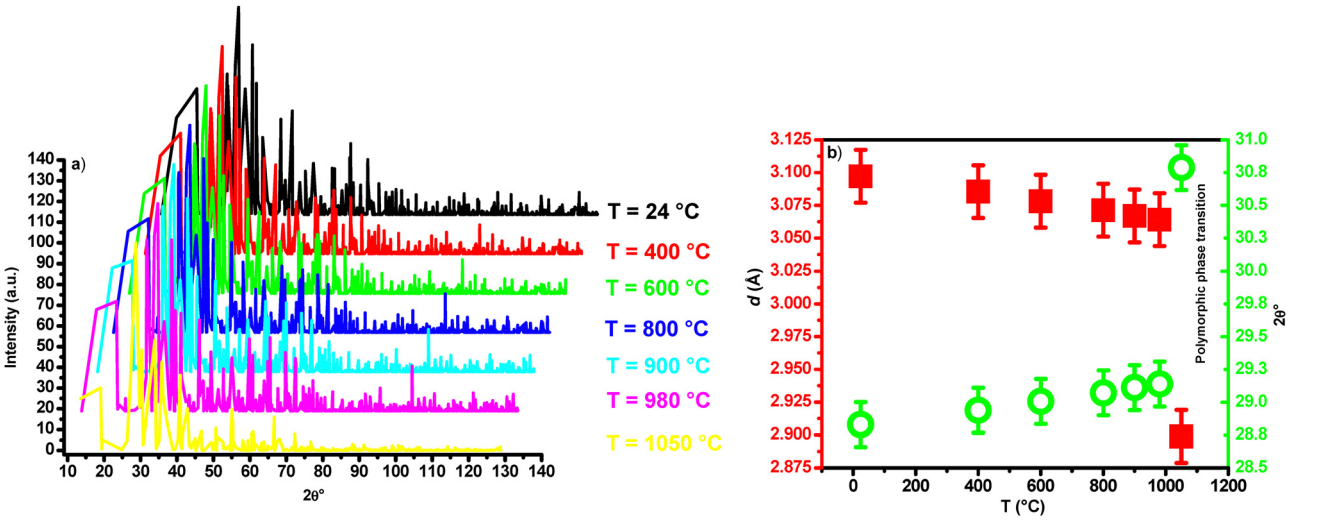

Fig. 1 Temperature-dependent X-ray diffraction (XRD) of orthoferrosilite ($FeSiO_3$). (a) Full XRD patterns simulated from the CIFs listed in Table 1. (b) Temperature evolution of the principal reflection indexed as (6 1 0) (at Cu K_α, λ = 1.5406 Å) and the corresponding interplanar spacing d(6 1 0) showing an abrupt change at ≈1050 °C associated with the orthorhombic (*Pbca*, #61) → monoclinic (*C*2/*c*, #15) first order polymorphic phase transition.

centered 2θ values. All measurements were performed in air. A full description of the experimental setup, including crystal dimensions, furnace calibration, and intensity correction procedures, is provided in the original work.[19,20] This dataset captures the progressive thermal expansion of the lattice and the first-order polymorphic transition occurring near 1050 °C, as confirmed by simulated X-ray diffraction patterns using VESTA software[26] (see Fig. 1a and b).

Key derived structural parameters—including lattice constants, unit cell volume (V_c), density (ρ), and atomic packing fraction (APF)—were calculated for each temperature and are compiled in Table 1. The density, a critical parameter for shielding, decreased from 4.00 g cm^{-3} at 24 °C to 3.86 g cm^{-3} at 980 °C. The three-dimensional crystal structure was visualized using VESTA software[28] to illustrate the interconnected network of FeO_6 octahedra and SiO_4 tetrahedra (Fig. 4).

2.2. Gamma-ray attenuation calculations

The gamma-ray shielding parameters for orthoferrosilite were computed across a broad energy spectrum (0.015–15 MeV) using the Phy-X/PSD software toolkit.[29] This range encompasses the photoelectric, Compton scattering, and pair production interaction regimes. For each temperature state defined by the crystallographic data, the following parameters were calculated:[1]

- Mass attenuation coefficient (MAC, μ/ρ): the probability of photon interaction per unit mass.
- Linear attenuation coefficient (LAC, μ): the absolute attenuation per unit thickness, obtained from the product $\mu = (\mu/\rho) \times \rho$. This is the primary engineering metric for shield design.
- Effective atomic number (Z_{eff}): a composite atomic number weighted by the electron fraction of each constituent element.
- Equivalent atomic number (Z_{eq}): the atomic number of a single element that would exhibit the same linear attenuation coefficient at a specific photon energy.

The temperature invariance of the chemical composition ($FeSiO_3$) ensures that any variation in these parameters is solely attributable to changes in density and atomic packing induced by thermal expansion.[19] In addition to the macroscopic parameters, the temperature-dependent evolution of cation polyhedral volumes (FeO_6 octahedra and SiO_4 tetrahedra) was extracted from the CIFs to elucidate the atomic-scale origin of the thermal expansion. The effective electron density (N_{eff}) for gamma-ray interactions was also calculated to decouple the effects of density change from intrinsic interaction cross-sections.

2.3. Uncertainty and precision of employed approaches

To ensure transparency and reproducibility, we report below the sensitivities and precisions associated with each methodological approach used in this work.

2.3.1. Crystallographic data (source uncertainty). The original high-temperature X-ray diffraction experiments by Sueno *et al.*[19] were performed on a synthetic single crystal of orthoferrosilite using Cu K_α radiation (λ = 1.5406 Å) on a Picker four-circle diffractometer equipped with a gas-flow furnace. Lattice parameters at each temperature were refined by least-squares fitting of 12–15 centered 2θ reflections. The reported precisions are:

- Lattice parameters (a, b, c): ±0.002–0.005 Å.
- Unit cell volume (V_c): ±0.2–0.5 Å^3.
- Density (ρ): ±0.002–0.005 g cm^{-3}.
- Atomic coordinates and displacement parameters: refined to conventional R-factors of 3–5%, indicating high structural fidelity.

These uncertainties are intrinsic to the source data and are carried forward into all derived parameters (APF, polyhedral volumes, and local electron densities).

2.3.2. Derived structural parameters. The following parameters were calculated directly from the CIF data using VESTA software[28] and custom spreadsheet calculations:

- Atomic packing fraction (APF): precision limited by original coordinate uncertainties; estimated relative uncertainty ±0.5–1%

- Polyhedral volumes (FeO_6, SiO_4): ±0.02–0.05 Å^3
- Local electron density (ρ_e) within polyhedra: ±0.01–0.03 e$^-$ Å^{-3}

All values are reported to three significant figures, consistent with the input data precision.

2.3.3. Gamma-ray attenuation calculations. The gamma-ray shielding parameters (MAC, LAC, Z_{eff}, Z_{eq}, N_{eff}) were computed using the Phy-X/PSD online software toolkit.[29] This platform utilizes fundamental atomic cross-section data from the EPICS2017 library, which is the current standard for photon interaction calculations. Benchmark studies have demonstrated that Phy-X/PSD yields mass attenuation coefficients with relative differences <1% compared to EPICS2017 and XCOM across most energy regimes.[23,24] Inherent uncertainties in the underlying cross-section data are estimated at:

- 1–2% in the Compton scattering regime (0.1–5 MeV)
- 2–3% in the photoelectric regime (<0.1 MeV), particularly near absorption edges
- < 1% in the pair production regime (>5 MeV)

Our computed values are reported to three significant figures, reflecting the combined precision of the input density data and the cross-section libraries.

2.3.4. Sensitivity to temperature. The observed density decrease of 3.2% between 25 °C and 800 °C is more than an order of magnitude larger than the combined experimental uncertainties (±0.1–0.2%). Similarly, the reduction in LAC at low energies (~9% at 1.0 MeV for the highest gamma dose) is well above the computational uncertainty envelope. Therefore, all trends and conclusions reported in this study are statistically significant and not limited by measurement or computational noise.

3. Results

3.1. Macroscopic structural evolution

The temperature-dependent crystallographic parameters of orthoferrosilite ($FeSiO_3$) are summarized in Table 1. Between 24 °C and 980 °C, the mineral retains its orthorhombic structure (space group *Pbca*, #61), exhibiting a progressive and anisotropic lattice expansion.[19] The unit cell volume increases by approximately 3.8% over this range, from 875.55 Å^3 to 908.25 Å^3. This thermal expansion leads to a corresponding decrease in both the calculated density (ρ) and the atomic packing fraction (APF). The density declines from 4.00 g cm^{-3} at 24 °C to 3.86 g cm^{-3} at 980 °C, while the APF—a measure of the volume fraction occupied by atoms—decreases from 0.668 to 0.644.

These trends are visualized in Fig. 2. The monotonic decrease in bulk density (Fig. 2a) and the associated increase in molar volume confirm the lattice loosening with rising temperature. Concurrently, the oxygen packing density (OPD, Fig. 2b), which represents the number of oxygen atoms per unit volume, shows a consistent decline. This reduction in OPD is particularly significant for gamma-ray shielding, as oxygen constitutes a major fraction of the electron-dense matrix. A marked discontinuity in all these parameters is observed at approximately 1050 °C, coinciding with the first-order polymorphic transition to a monoclinic (*C*2/*c*) structure, as independently evidenced by the shift in the principal XRD reflection (Fig. 1b).[19,20]

3.2. Atomic-scale structural response

The macroscopic lattice expansion and density reduction described in Section 3.1 originate from distinct, anisotropic changes at the atomic scale. The temperature evolution of the cation coordination polyhedra is quantified in Table 2, which lists the volumes of the $Fe1O_6$ and Fe_2O_6 octahedra and the SiA and SiB tetrahedra, along with their corresponding local electron densities (ρ_e, in e$^-$ Å^{-3}).[23]

A pronounced and consistent trend is observed: the Fe-centered octahedra expand substantially with increasing temperature, while the Si-centered tetrahedra undergo a slight contraction. The mean thermal expansion coefficients (MTEC) for the Fe1 and Fe2 sites are +5.0 × 10^{-5} K^{-1} and +8.4 × 10^{-5} K^{-1}, respectively.[19] In contrast, the MTEC values for the SiA and SiB tetrahedra are negative, approximately −0.7 × 10^{-5} K^{-1}. This differential

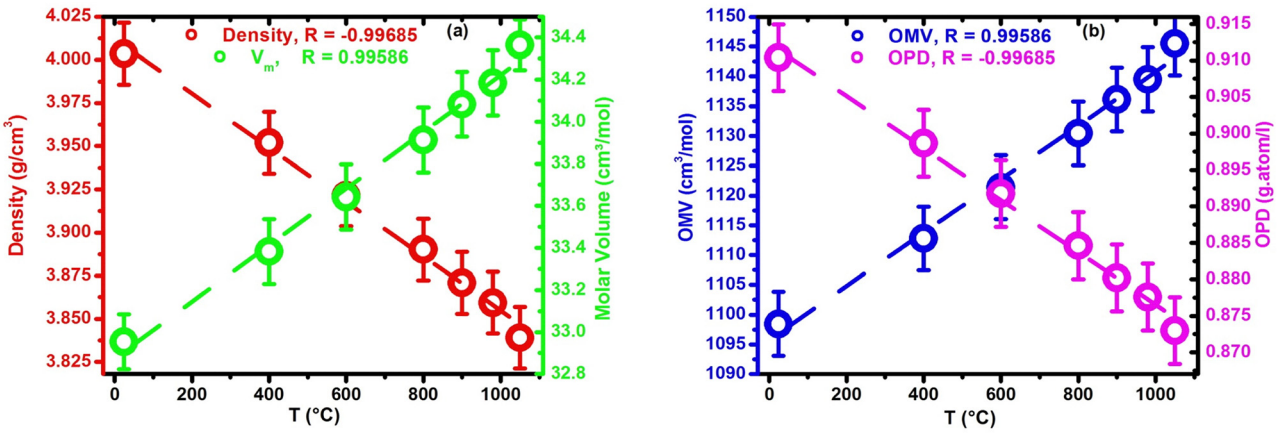

Fig. 2 Temperature dependence of (a) bulk density (ρ) and molar volume (V_m), and (b) oxygen molar volume (OMV) and oxygen packing density (OPD) for orthoferrosilite. The discontinuity near 1050 °C corresponds to the orthorhombic-to-monoclinic phase transition. The monotonic decrease in ρ and OPD with temperature is the primary driver for the reduction in gamma-ray shielding efficacy.

Table 2 Temperature evolution of cation polyhedral volumes in orthoferrosilite is shown in the Table. The data quantify the anisotropic thermal response: the FeO_6 octahedra (sites Fe1 and Fe2) expand significantly, while the SiO_4 tetrahedra (sites SiA and SiB) contract slightly. The mean thermal expansion coefficients (MTEC, in 10^{-5} K^{-1}) for the 24–980 °C interval are given in the final column. Data were taken from ref. 19

Polyhedral volume (Å^3) and local density (e^- Å^{-3}) at temperature (°C)													
	24 °C		400 °C		600 °C		800 °C		900 °C		980 °C		
Cation site	V_{hedral}	ρ_e	V_{hedral}	ρ_e	V_{hedral}	ρ_e	V_{hedral}	ρ_e	V_{hedral}	ρ_e	V_{hedral}	ρ_e	MTEC[a] (10^{-5} K^{-1})
Fe1	12.804	6.56	13.039	6.44	13.189	6.37	13.270	6.33	13.318	6.31	13.432	6.25	5.0133
Fe2	16.851	4.95	17.240	4.87	17.569	4.78	17.837	4.71	18.074	4.65	18.175	4.62	8.4033
SiA	2.182	22.92	2.180	22.94	2.165	23.10	2.174	23.00	2.177	22.97	2.162	23.13	−0.6710
SiB	2.233	22.39	2.221	22.51	2.216	22.56	2.199	22.74	2.198	22.75	2.187	22.86	−0.7136

[a] Mean thermal expansion coefficient.

expansion—where the larger FeO_6 polyhedra expand at a rate an order of magnitude greater than the contraction of the SiO_4 units—is the direct structural driver of the net increase in unit cell volume.[20–22]

Differential thermal expansion governs density reduction through the dominant volume expansion of Fe_2O_6 octahedra, which outweighs the minor contraction of SiO_4 tetrahedra, leading to net unit cell expansion and density dilution.[19] Structural stability is concurrently maintained by straightening of the silicate chains and distortion flexibility of the M2 site, which together accommodate octahedral expansion without disrupting the *Pbca* framework.[20] Thus, the same mechanism that degrades shielding density also preserves crystallographic integrity—a critical duality for high-temperature shielding applications.[21,22]

The local electron density within each polyhedron, calculated from its total electron count and volume, provides critical insight into the evolving shielding environment. As the FeO_6 octahedra expand, their local electron density decreases systematically; for the Fe2 site, it declines from 4.95 e^- Å^{-3} at 24 °C to 4.62 e^- Å^{-3} at 980 °C, a reduction of ∼6.7%. This represents a significant dilution of electron density around the high atomic number (Z = 26) Fe^{2+} cations, which are the primary agents for photoelectric absorption. Conversely, the slight contraction of the SiO_4 tetrahedra leads to a marginal increase (∼1–2%) in their local electron density. However, given the lower atomic number of silicon (Z = 14), this increase has a comparatively minor effect on overall photon attenuation.

This atomic-scale analysis reveals that thermal expansion in orthoferrosilite is not uniform but is dominated by the expansion of the FeO_6 octahedra. This process directly reduces the density of the electron cloud most responsible for low-energy photon absorption, providing a mechanistic link between the crystallographic changes and the subsequent evolution of shielding performance.

3.3. Gamma-ray shielding parameters

The intrinsic gamma-ray interaction parameters of orthoferrosilite, calculated across the energy spectrum from 0.015 to 10 MeV, are compiled in Table 3. The MAC exhibits the characteristic strong energy dependence, decreasing over two orders of magnitude from 27.0 cm^2 g^{-1} at 15.0 keV to 0.079 cm^2 g^{-1} at 10 MeV. This trend reflects the transition from dominant photoelectric absorption at low energies to Compton scattering and pair production at higher energies.

The derived parameters—the Z_{eff}, Z_{eq}, and N_{eff}—provide further insight into the interaction physics. As shown in Table 3, Z_{eff} decreases from 23.1 at 15 keV to a minimum of 12.9 around 8–10 MeV. This decline illustrates the shifting dominance from photoelectric interactions, which are highly sensitive to the high-Z Fe cations, to Compton scattering, which depends on the total electron density of the material. Concurrently, N_{eff} decreases from 5.27 × 10^{23} e^- cm^{-3} to 2.93 × 10^{23} e^- cm^{-3} over the same energy range. $N_{eff}(E)$ represents the density of electrons effective in attenuation at a specific photon energy E; at low energies, the interaction is weighted heavily toward the inner electrons of iron, resulting in a higher effective density.[13]

A pivotal finding of this study is the temperature invariance of these intrinsic parameters. For orthoferrosilite, the values of Z_{eff}, Z_{eq}, and N_{eff} at any given photon energy remain constant across the entire studied temperature range (24–980 °C). This invariance stems from the fixed chemical composition (*i.e.*, $FeSiO_3$); the fundamental photon interaction cross-sections of the constitu-

Table 3 Photon interaction parameters of orthoferrosilite ($FeSiO_3$), including the mass attenuation coefficient (MAC), effective atomic number (Z_{eff}), equivalent atomic number (Z_{eq}), and effective electron density (N_{eff}) calculated at photon energies ranging from 0.015 MeV to 15 MeV are shown in the Table. The data encompass the photoelectric absorption, Compton scattering, and pair production energy regions, providing insight into the radiation shielding performance of $FeSiO_3$ across a broad photon energy spectrum. The values for Z_{eff}, Z_{eq}, and N_{eff} are representative and were found to be invariant with temperature across the studied range (24–980 °C)

Energy (MeV)	MAC (cm^2 g^{-1})	Z_{eff}	Z_{eq}	N_{eff} × 10^{23}
0.0150	27.032	23.1	19.18	5.27
0.020	12.136	23.1	19.44	5.27
0.030	3.904	22.68	19.73	5.18
0.040	1.78	21.83	19.89	4.98
0.050	0.999	20.72	20.01	4.73
0.06	0.648	19.53	20.1	4.46
0.200	0.134	13.48	20.53	3.08
0.300	0.108	13.07	20.62	2.98
0.400	0.095	12.95	20.67	2.95
0.500	0.086	12.89	20.69	2.94
5.00	0.03	13.36	16.65	3.05
6.00	0.028	13.52	16.62	3.09
8.00	0.026	13.83	16.58	3.16
10.00	0.026	14.08	16.56	3.21

ent atoms are not altered by thermal lattice expansion. Consequently, the mass attenuation coefficient (μ/ρ), which is directly related to these parameters, is also temperature-independent.[24]

The three-dimensional structural framework in which these interactions occur is illustrated in Fig. 4, showcasing the interconnected network of FeO_6 octahedra and SiO_4 tetrahedra characteristic of the orthopyroxene structure.[28] In this framework, two distinct types of silicate tetrahedral chains---designated A and B—are linked through non-bridging oxygen atoms to FeO_6 octahedral strips, where Fe^{2+} occupies both the smaller, more regular M1 (Fe1) site and the larger, more distorted M2 (Fe2) site.[19] This topology, represented in the 'I-beam' model of pyroxenes, highlights how tetrahedral chain rotations[20] and octahedral stacking sequences[21,22] govern the structural response to thermal and radiative stimuli, such as those induced by gamma irradiation.[24]

While the intrinsic interaction strength per gram (μ/ρ) is constant, the macroscopic LAC, which determines the required shield thickness, depends directly on density: $\mu(T) = (\mu/\rho) \times \rho(T)$. The consequence of thermal expansion on this critical engineering metric is visualized in Fig. 3. The surface plot (Fig. 3a) shows the combined dependence of LAC on both photon energy and temperature, with a clear overall decrease in LAC values as temperature increases. This decline is particularly pronounced at lower energies, as emphasized in Fig. 3b for the 0.015–0.040 MeV range, where the photoelectric effect on Fe dominates.[24]

The direct, linear relationship between the reduction in LAC and the increasing temperature (or decreasing of APF) is quantified in Fig. 5. The linear fits demonstrate that the loss of shielding performance is a predictable and scalable function of the thermal expansion quantified in Sections 3.1 and 3.2. This provides a straightforward engineering correlation: the shielding effectiveness of an orthoferrosilite barrier at elevated temperatures can be accurately estimated by accounting for its thermally reduced density.[11]

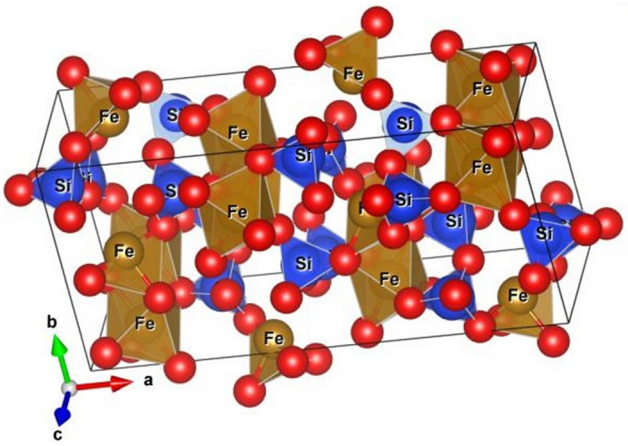

Fig. 4 Three-dimensional structural model of orthoferrosilite crystal with orthorhombic system (space group *Pbca*, #61), showcasing characteristic polyhedral arrangements. The framework consists of interconnected SiO_4 tetrahedra and FeO_6 octahedra, exhibiting distinct bond lengths and coordination geometries. The visualization, generated using VESTA software,[28] highlights the structural complexity and diversity of atomic environments in orthoferrosilite crystal.

3.4. Comparative shielding performance with standard glass systems

To evaluate the radiation shielding capability of orthoferrosilite relative to established materials, its MAC were compared with five standard glass systems commonly used in radiation shielding applications, as presented in Table 4. At the lowest photon energy examined (0.015 MeV), orthoferrosilite exhibits a MAC of 27.032 $cm^2\ g^{-1}$, which is substantially higher than Type A (borate-based: 11.817 $cm^2\ g^{-1}$), Type B (tellurite-based:

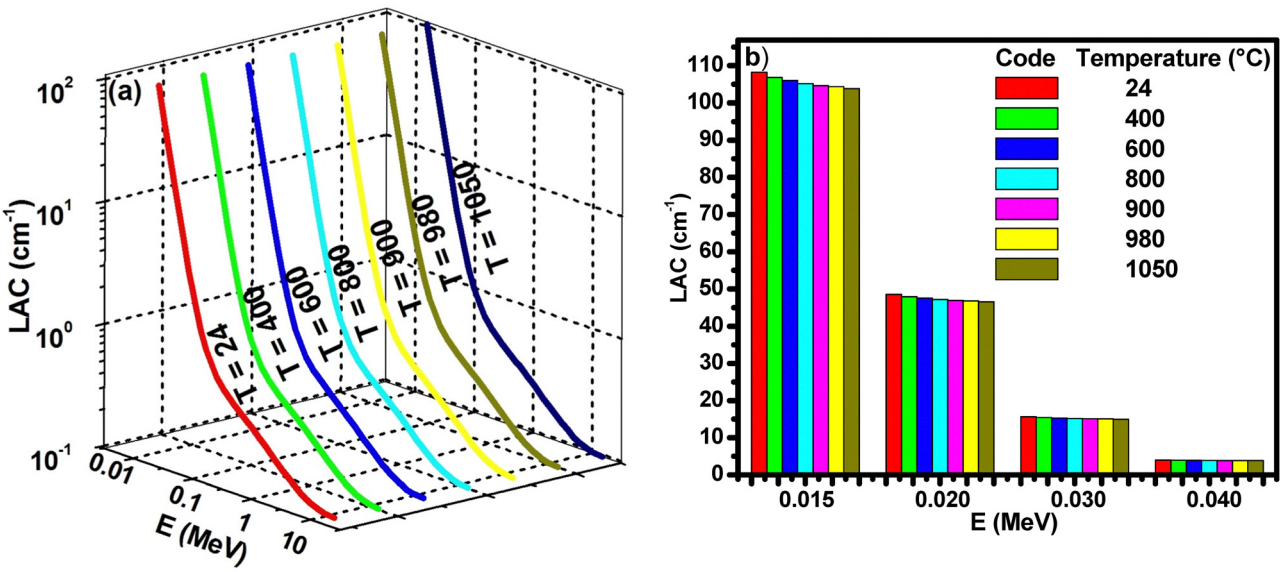

Fig. 3 (a) Three-dimensional surface plot of the LAC for orthoferrosilite as a function of photon energy and temperature. (b) Cross-sections of the surface at four low energies, highlighting the consistent decrease in LAC with increasing temperature across the photoelectric dominance region.

12.007 $cm^2\ g^{-1}$), Type C (phosphate-based: 8.640 $cm^2\ g^{-1}$), and RS-253-G18 (silicate-based: 13.959 $cm^2\ g^{-1}$) glasses. Only the heavy metal oxide glass RS-360 (106.855 $cm^2\ g^{-1}$) surpasses orthoferrosilite at this energy, attributable to its high content of high-atomic-number elements such as lead or bismuth. This demonstrates that orthoferrosilite offers superior low-energy photon absorption compared to most standard shielding glasses, despite being a crystalline silicate rather than a heavily doped amorphous system. At intermediate energies (0.5–5.0 MeV), where Compton scattering dominates, orthoferrosilite maintains MAC values (0.086–0.030 $cm^2\ g^{-1}$) comparable to the glass systems, with all materials converging to similar values ($\sim$0.030 $cm^2\ g^{-1}$) at 5.0 MeV. At 15 MeV, orthoferrosilite (0.025 $cm^2\ g^{-1}$) remains competitive with the glass systems (0.022–0.055 $cm^2\ g^{-1}$). Critically, the MAC values for orthoferrosilite are temperature-invariant across the entire 24–980 °C range, meaning that even at elevated operating temperatures, its intrinsic photon attenuation capability per unit mass is preserved. The glass systems, by contrast, are reported only at room temperature and would likely experience performance degradation at elevated temperatures due to thermal expansion or structural changes.

For practical shielding design, the LAC and the corresponding HVL and TVL are essential engineering parameters. Table 5 compares these parameters at 0.015 MeV for orthoferrosilite at room temperature with the five glass systems. Orthoferrosilite exhibits a LAC of 108.224 cm^{-1}, which is substantially higher than Type A (29.543 cm^{-1}), Type B (30.016 cm^{-1}), Type C (15.121 cm^{-1}), and RS-253-G18 (35.595 cm^{-1}) glasses. Only RS-360 (267.138 cm^{-1}) exceeds orthoferrosilite, consistent with its higher MAC and greater density. The HVL—the thickness required to reduce photon intensity by half—is inversely proportional to LAC. Orthoferrosilite achieves an HVL of only 0.006 cm (60 μm) at 0.015 MeV, meaning a mere 60-micron layer attenuates 50% of incident 15 keV photons. This is significantly thinner than the HVL values for Type A (0.023 cm), Type B (0.023 cm), Type C (0.046 cm), and RS-253-G18 (0.019 cm) glasses. RS-360, with its extremely high LAC, exhibits an HVL of just 0.003 cm (30 μm). Similarly, the TVL—thickness for 90% attenuation—is 0.021 cm (210 μm) for orthoferrosilite, compared to 0.078 cm, 0.077 cm, 0.152 cm, and 0.065 cm for Type A, B, C, and RS-253-G18 glasses, respectively. These results demonstrate that orthoferrosilite

Table 4 Comparison of mass attenuation coefficients (MAC, in $cm^2\ g^{-1}$) for orthoferrosilite ($FeSiO_3$) at temperatures between 24 °C and 980 °C with five standard glass systems commonly used in radiation shielding applications are shown in the Table. The temperature invariance of MAC in orthoferrosilite is highlighted, demonstrating that its intrinsic photon attenuation per unit mass remains unchanged despite thermal expansion. All glass data are reported at room temperature. Glass types: Type A (borate-based), Type B (tellurite-based), Type C (phosphate-based), RS-253-G18 (silicate-based), RS-360 (heavy metal oxide glass)

E (MeV)	$FeSiO_3$	Type A glass	Type B glass	Type C glass	RS-253-G18	RS-360
0.015	27.032	11.817	12.007	8.640	13.959	106.855
0.5	0.086	0.087	0.087	0.087	0.088	0.158
1.0	0.062	0.063	0.063	0.063	0.063	0.071
5	0.030	0.030	0.030	0.029	0.029	0.042
15	0.0.025	0.024	0.024	0.022	0.024	0.055

Table 5 Comparison of the linear attenuation coefficient (LAC, in cm^{-1}), half-value layer (HVL, in cm), and tenth-value layer (TVL, in cm) at photon energy E = 0.015 MeV for orthoferrosilite ($FeSiO_3$) at T = 24 °C with five standard glass systems commonly used in radiation shielding applications are shown in the Table. All glass data are reported at room temperature. Glass types: Type A (Borate-based), Type B (tellurite-based), Type C (phosphate-based), RS-253-G18 (silicate-based), RS-360 (heavy metal oxide glass)

Parameter	$FeSiO_3$	Type A glass	Type B glass	Type C glass	RS-253-G18	RS-360
LAC	108.224	29.543	30.016	15.121	35.595	267.138
HVL	0.006	0.0235	0.023	0.046	0.0195	0.026
TVL	0.021	0.078	0.077	0.152	0.065	0.009

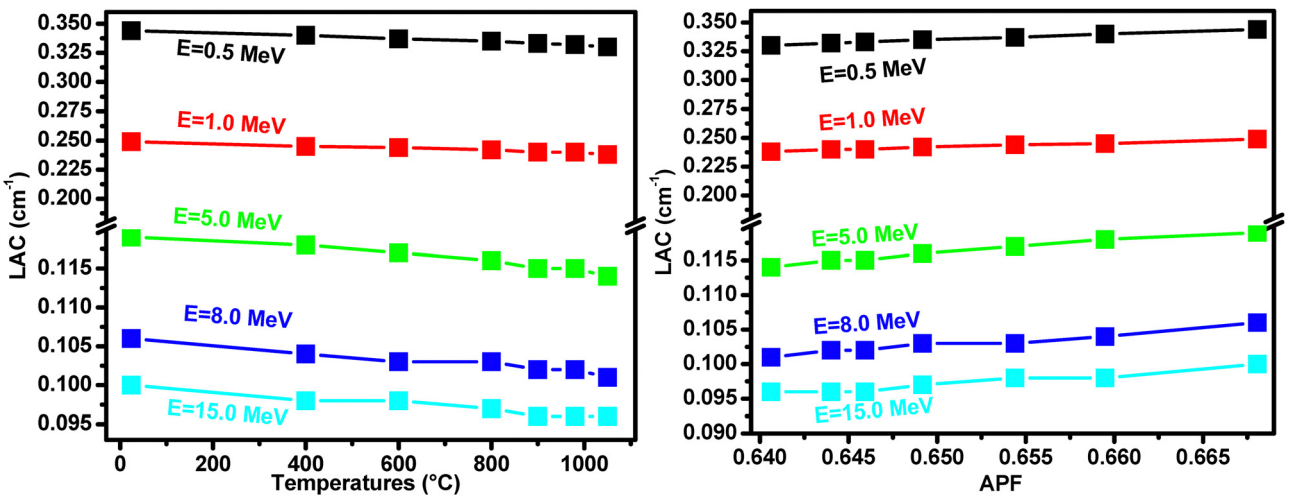

Fig. 5 The LAC plots at selected photon energies with (a) temperature, and (b) APF. The direct proportionality confirms that the loss of shielding performance is quantitatively driven by thermal lattice expansion and the associated reduction in atomic packing density.

offers exceptionally compact shielding at low photon energies, requiring only micrometer-scale thicknesses for effective attenuation—comparable to heavy metal oxide glasses and far superior to standard borate, tellurite, phosphate, and silicate glass systems. This makes orthoferrosilite particularly attractive for applications where space and weight are critical constraints, such as space exploration or portable shielding devices.

4. Discussion

4.1. Linking atomic structure to macroscopic properties

The observed macroscopic decrease in density (Fig. 2a) is a direct structural consequence of the differential thermal expansion between the FeO_6 octahedra and SiO_4 tetrahedra within the orthopyroxene framework. As detailed in Section 3.2, the mean Fe–O bond lengths—particularly those in the Fe2 (M2) polyhedron—exhibit pronounced thermal expansion (Table 2), consistent with the high-temperature behavior reported for orthoferrosilite by Sueno *et al.*[19] In contrast, the Si–O bonds and tetrahedral volumes show only a slight contraction or near-zero thermal expansion.[19,20]

This asymmetric expansion mechanism leads to an overall increase in unit cell volume dominated by the expansion of the octahedral layer. The resulted loosed structural manifests macroscopically as a measurable decrease in density.[26] Notably, the Fe2 site which is more distorted and exhibits variable coordination (shifting from 6- to 7-coordinate at intermediate temperatures) contributes disproportionately to the volumetric expansion, underscoring the role of cation site distortion in mediating thermal response.[26] Thus, the density trend in Fig. 2a can be interpreted as a macroscopic fingerprint of the underlying crystal-chemical response: the large, flexible FeO_6 octahedra expand under thermal or radiative excitation, while the rigid SiO_4 tetrahedra remain largely invariant, leading to net volume increase and density reduction.

4.2. Impact on photon attenuation

The observed reduction in the LAC (see Fig. 5) with increasing temperature or irradiation dose can be directly attributed to the decrease in material density and atomic packing fraction described in Section 3.1. As established in Section 3.2, this density decrease stems from the pronounced thermal expansion of FeO_6 octahedra—particularly the Fe2 polyhedron—which outweighs the minor contraction of SiO_4 tetrahedra, consistent with the behavior of orthoferrosilite under thermal stress.[15–17]

Critically, despite the volumetric expansion and decrease in bulk density, both the N_{eff} and Z_{eff} remain essentially constant across the measured conditions (see Table 3). This invariance confirms that the observed degradation in shielding performance is not due to any change in the intrinsic photon interaction probabilities per atom (*e.g.*, photoelectric, Compton scattering, or pair production cross-sections), but rather is a purely density-dilution effect.

In other words, the orthopyroxene structure expands, increasing the average spacing between atoms without altering their electronic configuration or identity. Thus, while the probability of interaction per atom remains unchanged, then the number of atoms per unit volume decreases, leading to a linear reduction in LAC. This relationship underscores that for orthoferrosilite-based shielding materials, maintaining structural density is paramount to preserving radiation attenuation performance under thermal or radiative environments.

4.3. Practical implications and phase stability

The thermal and structural responses observed in orthoferrosilite have direct implications for its stability and performance as a radiation shielding material in non-ambient environments.

4.3.1. Phase stability under thermal stress. Orthoferrosilite exhibits no phase transformations up to 980 °C,[19] confirming its stability within the *Pbca* orthopyroxene structure across a broad temperature range. This is advantageous for applications requiring thermal cycling, as the material will not undergo disruptive crystallographic transitions that could induce micro-cracking or property degradation. However, the pronounced and differential expansion of FeO_6 octahedra—especially the Fe2 site—relative to the nearly invariant SiO_4 tetrahedra suggests that internal coherency stresses may develop at grain boundaries or in composite systems with different thermal expansion coefficients.[20] In polycrystalline or composite shielding forms, these stresses could affect mechanical integrity over repeated thermal cycles.[21,22]

4.3.2. Impact on shielding performance in thermal environments. The reduction in density due to thermal expansion directly degrades photon attenuation performance, as shown by the decreasing linear attenuation coefficient (Fig. 5). For design purposes, this implies that shielding thickness must be de-rated at elevated temperatures to compensate for density dilution. Engineers should incorporate temperature-dependent density models—based on the mean thermal expansion coefficients of the orthopyroxene structure as discussed in Sueno *et al.*[19]—into shielding calculations for high-temperature applications.

4.3.3. Gamma environment considerations. While pure thermal expansion is reversible, gamma irradiation may induce cumulative structural damage (discussed further in Section 4.4). In a mixed radiation-thermal environment—such as in nuclear reactors or space applications—synergistic effects could accelerate property changes. For example, radiation-induced point defects may lower the activation energy for thermal diffusion,[30] enhancing creep or sintering processes that permanently alter microstructure and density.[31]

4.3.4. Material design recommendations. To mitigate these effects in practical shielding systems, we recommend:

1. Stabilizing the M2 site: partial substitution of Fe^{2+} with smaller, higher-valence cations (*e.g.*, Mg^{2+}, Al^{3+}) could reduce octahedral distortion and lower thermal expansively.

2. Composite approach: embedding orthoferrosilite within a matrix with matched thermal expansion and high radiation tolerance (*e.g.*, certain glass-ceramics or oxides) to buffer internal stresses and maintain macroscopic density.

3. Operational limits: defining temperature and dose windows where structural changes remain largely reversible, ensuring long-term performance stability.

Thus, while orthoferrosilite possesses favorable intrinsic attenuation properties and high thermal phase stability, its performance in real environments is limited by thermally-induced density reduction and potential radiation damage. Addressing these through material design and operational planning is essential for its successful deployment as a functional radiation shield.

4.4. Reversibility of structural changes: gamma *versus* thermal effects

While both thermal and gamma-induced environments produce measurable decreases in density and attenuation performance, the fundamental mechanisms—and thus the potential for recovery—differ significantly. Understanding this distinction is crucial for predicting the long-term performance and lifetime of orthoferrosilite-based shielding.

4.4.1. Thermally-induced changes: largely reversible. The structural changes driven by heating—primarily the expansion of the FeO_6 octahedra and the straightening of the SiO_4 tetrahedral chains—are thermodynamic, equilibrium processes. As demonstrated by Sueno *et al.*,[19] these changes are smooth, regular, and exhibit no phase transformations up to 980 °C. The expansion is governed by anharmonic lattice vibrations and is fully described by mean thermal expansion coefficients.[19,30,31] Upon cooling, the structure relaxes back along the same energetic pathway, making the associated density reduction and shielding degradation largely reversible. This reversibility and re-orientation is a key advantage for applications involving thermal cycling, as the material's intrinsic shielding properties can be restored upon return to ambient conditions.[31–33]

4.4.2. Gamma-induced changes: potentially irreversible. In contrast, structural modifications from gamma irradiation result from non-equilibrium, athermal processes. High-energy photons can:

1. Cause electronic excitations and ionization: this can lead to localized charge imbalances, particularly affecting Fe^{2+} ions and potentially altering their oxidation state (*e.g.*, $Fe^{2+} \rightarrow Fe^{3+}$).[19]

2. Generate atomic displacements: through Compton scattering or photoelectric recoil, atoms (especially lighter O and Si) can be knocked from their lattice sites, creating Frenkel pairs (*i.e.*, vacancies and interstitials).[38]

3. Produce transient thermal spikes: localized energy deposition can create fleeting, extreme temperature gradients, leading to quenched-in disorder.[20]

These processes create metastable point defects and lattice distortions that are not part of the material's equilibrium phase diagram. Consequently, gamma-induced density reduction may stem not only from simple lattice expansion but from the accumulation of vacancies and disordered regions. This type of damage is often irreversible or only partially recoverable through annealing, as it requires diffusion and recombination of defects—processes with higher activation energies than simple thermal vibration.[36]

Based on extensive literature on gamma-irradiated silicates, the most plausible microstructural defects in orthoferrosilite are Frenkel-type defects on the oxygen sublattice—specifically, diamagnetic oxygen vacancies (precursors to E' centers) and charge-compensating interstitial oxygen atoms.[37,38] These point defects arise from radiolytic rupture of Si–O–Si bonds within the rigid SiO_4 tetrahedral framework, a process well-documented in α-quartz and amorphous silica.[37,38] Gamma radiation has been shown to be the dominant contributor to Frenkel pair formation in silicate systems under mixed-field irradiation.[38]

Each Frenkel pair introduces local volume expansion without altering chemical composition or elemental identity.[38] The oxygen vacancy creates a missing atom site, while the interstitial oxygen occupies extra volume elsewhere in the lattice. This results in swelling at constant mass and density dilution, fully consistent with our observation that Z_{eff} and N_{eff} remain invariant under irradiation (no change in composition or electron density per atom).[37,39]

Unlike thermally-induced lattice expansion—which is entropy-driven, equilibrium, and fully reversible upon cooling—these gamma-induced defects are metastable at room temperature.[38,39] They require thermal activation to recombine; isochronal annealing studies in irradiated SiO_2 demonstrate that significant defect recovery occurs only above 500–600 K.[37,39] At elevated doses or under prolonged irradiation, mobile interstitials may aggregate into clusters or become trapped at impurity sites, further stabilizing the damage and rendering recombination kinetically hindered.[35]

In orthoferrosilite, the FeO_6 octahedra are less directly affected by radiolytic bond rupture but are expected to expand elastically to accommodate the swelling and strain fields originating from the damaged tetrahedral sublattice. This indirect expansion further contributes to density dilution.[37–39]

Direct experimental verification of these proposed defects in orthoferrosilite—using electron paramagnetic resonance (EPR) to detect E' centers,[35] Raman spectroscopy to monitor Si–O–Si network distortion,[36] and positron annihilation spectroscopy (PAS) to probe vacancy-type defects—is planned as future work.[37] Post-irradiation annealing studies will also be conducted to quantify the reversibility fraction and determine activation energies for defect recombination.[38]

4.4.3. Distinguishing the mechanisms experimentally. The reversibility can be probed through post-irradiation annealing studies. If the decreased LAC recovers fully after annealing at moderate temperatures (*e.g.*, 400–600 °C), the damage is likely dominated by reversible, thermal-like expansion. If the recovery is incomplete, it indicates accumulated irreversible damage. Furthermore, techniques like Mössbauer spectroscopy[40] could detect changes in Fe oxidation state, and Raman spectroscopy[41] could reveal permanent distortion or breakage of Si–O bonds in the tetrahedral chains—both signatures of irreversible radiation damage absent in pure thermal treatment.[34]

4.4.4. Implications for long-term performance. In practical terms, the reversibility of structural changes dictates the long-term stability of orthoferrosilite as a radiation shield. In purely thermal environments, shielding degradation is predictable, cyclic, and largely recoverable upon cooling. In contrast, under sustained gamma irradiation, performance may degrade

cumulatively and permanently with accumulated dose due to irreversible defect accumulation. In mixed-field environments—such as nuclear reactors or space applications---synergistic effects are likely, where radiation-induced defects can enhance atomic diffusion or lower the activation energy for permanent microstructural changes, such as pore formation or phase segregation, thereby accelerating the irreversible loss of shielding efficacy.

Prolonged gamma exposure introduces athermal, metastable defects (primarily oxygen Frenkel pairs in the SiO_4 tetrahedral framework) that do not fully recover during thermal cycling.[35] When combined with thermal cycling, these defects can accumulate irreversibly, leading to progressive density dilution and permanent degradation of the LAC.[36,37] Additionally, radiation-enhanced diffusion may accelerate microstructural changes such as pore formation or phase segregation,[37] further compromising long-term shielding reliability.[36] Therefore, under mixed thermal and gamma environments, shielding performance degrades cumulatively and non-recoverably, unlike the reversible behavior observed under thermal cycling alone.[38]

Therefore, while orthoferrosilite shows promise for variable-temperature applications due to its reversible thermal expansion. Its use in high-dose radiation environments requires further investigation into defect tolerance and possible saturation doses beyond which damage becomes catastrophic for shielding effectiveness applications.

5. Conclusions and future work

This study has systematically investigated the response of synthetic orthoferrosilite to thermal and gamma-ray environments, linking atomic-scale structural behavior to macroscopic radiation shielding performance. The principal findings are as follows:

1. The observed reduction in density and LAC is primarily a density-dilution effect, driven by the pronounced thermal expansion of FeO_6 octahedra which outweighs the slight contraction of the rigid SiO_4 tetrahedra. The density decreased by 3.2% between 25–800 °C, with Fe_2O_6 octahedral volume expanding by 7.9% (MTEC = $+8.4 \times 10^{-5}$ K^{-1}) while SiO_4 tetrahedra contracted by $\sim$2% (MTEC = -0.7×10^{-5} K^{-1}), leading to a 6.7% dilution of local electron density around Fe^{2+} cations.

2. The invariant effective atomic number (Z_{eff}) and electron density (N_{eff}) confirm that the degradation in photon attenuation is not due to changes in intrinsic interaction cross-sections, but solely to the decrease in atomic packing.

3. A critical distinction exists in the reversibility of structural change: thermally-induced expansion is largely reversible, whereas gamma-induced damage may lead to cumulative, permanent defects, posing a greater risk for long-term shielding applications.

Future work should focus on clarifying the mechanisms and mitigating the observed degradation:

- Post-irradiation annealing studies: to experimentally distinguish reversible thermal expansion from irreversible radiation damage by monitoring the recovery of density and LAC.
- *In situ* structural characterization: using techniques such as high-temperature X-ray diffraction under gamma irradiation to directly observe defect formation and phase stability in real time.
- Compositional engineering: investigating the effect of cation substitution (*e.g.*, Mg^{2+}, Al^{3+} for Fe^{2+}) on reducing octahedral distortion and thermal expansion, thereby improving dimensional and shielding stability.
- Composite development: exploring the integration of orthoferrosilite into ceramic or glass-ceramic matrices designed to buffer thermal stresses and limit defect mobility under irradiation.

By addressing these points, the potential of orthopyroxene-based materials can be further optimized for reliable use in advanced shielding systems operating under combined thermal and radiative loads.

Conflicts of interest

There are no conflicts to declare.

Data availability

The datasets generated and/or analyzed during the current study are available from the corresponding author upon reasonable request. All relevant computational input files, raw data, and processed results will be shared with editors or reviewers if required for verification purposes.

Acknowledgements

Z. Y. Khattari would like to thank The Hashemite University for the generous financial support. During the preparation of this work the author used *ChatGPT/OpenAI* in order to improve the manuscript English language and grammar. After using this tool/service, the authors reviewed and edited the content as needed and take full responsibility for the content of the publication.

References

1 A. B. Chilton, J. K. Shultis and R. Faw, *Principles of Radiation Shielding*, Prentice-Hall, Englewood Cliffs, New Jersey, 1st edn, 1984.
2 K. Kovler, *Constr. Build. Mater.*, 2011, **25**, 3404–3409.
3 K. G. Field, I. Remec and Y. Le Pape, *Nucl. Eng. Des.*, 2015, **282**, 126–143.
4 A. S. Ouda, *Prog. Nucl. Energy*, 2015, **79**, 48–55.
5 P. Mishra, S. Ali, R. Kumar and S. Shekhar, *J. Trace Elem. Miner.*, 2025, **14**, 100259.
6 L. Zhang, Z. Song, Q. Qin, L. He, J. Tian, Y. Yu, Y. Mu, L. Zhong, Z. Cui and J. Gan, *Comp. Biochem. Physiol., Part C: Toxicol. Pharmacol.*, 2025, **298**, 110331.

7 J. Li, N. Sheng, H. Jin, X. Wei, Y. Xu and J. Liu, *Mater. Chem. Phys.*, 2026, **350**, 131915.
8 M. Rathee and A. Misra, *Process Saf. Environ. Prot.*, 2025, **200**, 107389.
9 S. K. Pal, Z. Y. Khattari, A. Dahshan and N. Mehta, *Radiat. Phys. Chem.*, 2025, **237**, 113004.
10 Z. Y. Khattari, *J. Am. Ceram. Soc.*, 2025, **108**, e20560.
11 Z. Y. Khattari, *Mater. Adv.*, 2026, **7**, 641–648.
12 G. P. Singh, J. Singh, P. Kaur, T. Singh and D. P. Singh, *J. Alloys Compd.*, 2025, **1021**, 179697.
13 M. Kh Hamad, *Ceram. Int.*, 2025, **51**, 9763–9977.
14 M. I. Sayyed, A. H. Almuqrin, R. Kurtulus, A. M. V. Javier-Hila, K. Kaky and T. Kavas, *Appl. Phys. A: Mater. Sci. Process.*, 2021, **127**, 243.
15 J. Thumma and R. K. Guntu, *Phys. B*, 2025, **716**, 417735.
16 K. V. Rao, M. Madhu, P. Ashok, N. R. K. Chand, S. Sripada, P. S. Prasad and C. S. Rao, *Silicon*, 2022, **14**, 9887–9899.
17 M. I. Sayyed, M. J. Zaiter, M. H. A. Mhareb, K. A. Mahmoud, S. Biradar, R. I. Mahdi and K. M. Kaky, *Opt. Mater.*, 2024, **154**, 115807.
18 S. E. Alawaideh, M. I. Sayyed, K. A. Mahmoud, M. Hanfi, M. A. Imheidat, K. M. Kaky, H. A. Thabit and M. Elsafi, *Radiat. Phys. Chem.*, 2024, **220**, 111720.
19 S. Sueno, M. Cameron and C. T. Prewitt, *Am. Mineral.*, 1976, **61**, 38–53.
20 M. Cameron, S. Sueno and C. T. Prewitt, *Am. Mineral.*, 1973, **58**, 594–618.
21 Y. Ohashi, PhD Thesis, Harvard University, 1973.
22 C. T. Prewitt and C. W. Burnham, *Earth Planet. Sci. Lett.*, 1972, **14**, 183–189.
23 S. Al-Omari, F. Afaneh, N. A. M. Alsaif, H. Al-Ghamdi, Y. S. Rammah and Z. Y. Khattari, *Radiat. Phys. Chem.*, 2024, **217**, 111527.
24 S. Al-Omari, F. Afaneh, R. A. Elsad, Y. S. Rammah and Z. Y. Khattari, *Radiat. Phys. Chem.*, 2024, **215**, 111377.
25 Crystallographic Information File (CIF), CCDC Software, Cambridge, UK, https://www.ccdc.cam.ac.uk/solutions/software/csd/.
26 Y. Ohashi and L. W. Finger, *Carnegie Inst. Washington, Year Book*, 1973, 72, 544–547.
27 Crystallography Open Database, https://www.crystallography.net/cod/result.php, (accessed 13 October 2025).
28 K. Momma and F. Izumi, *J. Appl. Crystallogr.*, 2011, **44**, 1272–1276.
29 E. Şakar, Ö. F. Özpolat, B. Alım, M. I. Sayyed and M. Kurudirek, *Radiat. Phys. Chem.*, 2020, **166**, 108496.
30 A. L. Frisillo and S. T. Buljan, *J. Geophys. Res.*, 1972, **77**, 7115–7117.
31 J. J. Papike, C. T. Prewitt, S. Sueno and M. Cameron, *Z. Kristallogr.*, 1973, **138**, 254–273.
32 Z. Y. Khattari, *Mater. Today Commun.*, 2025, **42**, 111521.
33 K. Zheng, Y. Wang, B. Chen, Y. Wu, M. Wang, K. Chen, X. Li, X. Li, A. Tang and Y. Wang, *Mater. Today Commun.*, 2024, **40**, 110017.
34 C.-C. Lin, *J. Phys. Chem. Solids*, 2004, **65**, 913–921.
35 H. H. Mahmud, A. Mansour and F. M. Ezz-Eldin, *J. Radioanal. Nucl. Chem.*, 2014, **302**, 261–272.
36 G. Buscarino, S. Agnello and F. M. Gelardi, *Phys. Rev. B: Condens. Matter Mater. Phys.*, 2006, **73**, 045208.
37 K. Kajihara, L. Skuja and H. Hosono, *J. Appl. Phys.*, 2013, **113**, 144103.
38 P. Vajda, *Rev. Mod. Phys.*, 1977, **49**, 481.
39 R. Tomon, *Denki Gakkai Zetsuen Zairyo Kenkyukai Shiryo*, 1987, **EIM-87**, 109–118.
40 W. D. Nesse and G. B. Baird, *Introduction to Mineralogy*, Oxford University Press, New York, 4th edn, 2022.
41 P. Gillet, *Phys. Chem. Miner.*, 1996, **23**, 263–275.